PCCP

Photoexcited energy relaxation and vibronic couplings in π-conjugated carbon nanorings

Journal:	*Physical Chemistry Chemical Physics*
Manuscript ID	CP-ART-03-2020-001452.R1
Article Type:	Paper
Date Submitted by the Author:	15-Jun-2020

Complete List of Authors:	Rodriguez-Hernandez, Beatriz; Universidad Nacional de Quilmes, CONICET, Departamento de Ciencia y Tecnologia Oldani, A; Universidad Nacional de Quilmes, CONICET, Departamento de Ciencia y Tecnologia Martinez-Mesa, Aliezer; Universidad de la Habana, DynAMoS (Dynamical processes in Atomic and Molecular Systems), Facultad de Fisica; Universidad Nacional de Quilmes, CONICET, Departamento de Ciencia y Tecnologia Uganda-Piña, Llinersy; Universidad de la Habana, DynAMoS (Dynamical processes in Atomic and Molecular Systems), Facultad de Fisica; Universidad Nacional de Quilmes, CONICET, Departamento de Ciencia y Tecnologia Tretiak, Sergei; Los Alamos National Laboratory, Theoretical Division Fernandez-Alberti, Sebastian; Universidad Nacional de Quilmes, CONICET, Departamento de Ciencia y Tecnologia

Photoexcited energy relaxation and vibronic couplings in π-conjugated carbon nanorings

B. Rodríguez-Hernández[a] N. Oldani[a], A. Martínez-Mesa[a,b], Ll. Uranga-Piña[a,b], S. Tretiak[c] and S. Fernandez-Alberti[a].

[a]Departamento de Ciencia y Tecnologia, Universidad Nacional de Quilmes/CONICET, B1876BXD Bernal, Argentina.
[b]DynAMoS (Dynamical processes in Atomic and Molecular Systems), Facultad de Física, Universidad de La Habana, San Lázaro y L, La Habana 10400, Cuba.
[c]Theoretical Division, Center for Nonlinear Studies (CNLS), and Center for Integrated Nanotechnologies (CINT), Los Alamos National Laboratory, Los Alamos, NM 87545, USA.

ABSTRACT

Conjugated carbon nanorings exhibit unique photophysical properties that, combined with their tunable sizes and conformations, make them suitable for a variety of practical applications. These properties are intimately associated to their strained, bent and sterically hindered cyclic structures. Herein we perform a comparative analysis of the photoinduced dynamics in carbon nanorings composed of nine phenyl units([9]CPP) and nine naphthyl units ([9]CN) respectively. The sterically demanding naphthyl units lead to large dihedral angles between neighboring units. Nevertheless, the ultrafast electronic and vibrational energy relaxation and redistribution is found to be similar for both systems. We observe that vibronic couplings, introduced by nonadiabatic energy transfer between electronic excited states, ensure the intramolecular vibrational energy redistribution through specific vibrational modes. The comparative impact of the internal conversion process on the exciton spatial localization and intra-ring migration indicates that naphthyl units in [9]CN achieve more efficient but less dynamical self-trapping compared to that of phenyl units in [9]CPP. That is, during the photoinduced process, the exciton in [9]CN is more static and localized than the exciton in [9]CPP. The internal conversion processes take place through a specific set of middle- to high-frequency normal modes, which directly influence the spatial exciton redistribution during the internal conversion, self-trapping and intra-ring migration.

I. INTRODUCTION

Carbon nanohoops, such as cycloparaphenylenes ([n]CPPs, see for example, **Figure 1(a)**)[1] consisting of *n* phenylene units linked at the *para* positions, have initially attracted the interest of the scientific community as seeds for carbon nanotube growth[2,3,4,5,6,7]. Nevertheless, they quickly became of interest by their own[8,9] due to their particular combination of bending strains, disorder and sterically hindrances. Altogether this significantly diversify and impact their optical absorption and emission properties[10]. The most unique feature of nanohoops is their side-dependent photophysical properties[11,12]. While the potential extent of conjugation increases with *n*, the associated relaxation of the strain leads to higher average torsional angles, decreasing the radial planarity of the π-system. Subsequently, in contrast to linear oligophenylenes, CPPs absorption maximum wavelengths are approximately independent of the π-conjugation length of the chain of phenyl units[10]. Nevertheless, their florescence is red shifted as [*n*]CPP hoop size decreases with a concomitant decrease of the quantum yield, a trend generally opposite to what is observed in their linear counterparts.

In the recent years, the synthesis of new conjugated carbon nanorings[8] has been providing a wide variety of chemical compounds with new structural and optical properties that can be conveniently tuned for specific optoelectronic applications[13]. Their potential scope of applications include solution-state and solid-state emitters[14,15,16,17], guest-uptake[9,18,19], organic field-effect transistors[20] and biological fluorophores[15], among others. The cyclic and curved conjugation allow for unique features that can be controlled by introducing changes in the number and chemical composition of their chromophore units,[21,22,23,24]. Besides, their covalent functionalization or complexation with guest molecules, such as fullerenes, provide them with an additional versatility for organic photovoltaic systems[19,25,26,27,28]. Nowadays, optical properties of nanohoops can easily be manipulated with atomic precision thanks to their stepwise organic synthesis. The successful synthesis of a large variety of modified CPPs provides us with the possibility to study their size dependent optical properties toward formulating rational design principles. Among these classes of nanorings, some illustrative examples are as follows: CPPs with acene units[29,30,31,2] , alkyl chains[32,33], tetraphenyl-substituted[34], with one phenyl unit linked in the meta-position[35], and so on.

The relationship between the strain and steric hindrances of bent structures and optical properties of nanorings can be altered by changing the arene units that compose them. This is the case of the recently synthetized [9]cyclo-1,4-naphthylene ([9]CN, see **Figure 1(a)**) by Itami et al.[36] composed of nine naphthyl units. [9]CN represents the first synthetized extended π-conjugated carbon nanoring presenting a number of structural and optical features different from those of [9]CPP (Fig. 1 inset).

The photoinduced electronic energy relaxation and redistribution in CPPs and related nanohoops[11,29,12,33] have been previously studied in detailed using a variety of electronic structure methodologies [37,38,39,40,41,42,43,44] including our Non-adiabatic Excited states Molecular Dynamics (NEXMD) approach[45,46,47]. Within the NEXMD framework, the exciton redistribution, self-trapping, and intra-ring migration during the internal conversion process can be elucidated through the analysis based on the evolution of the electronic transition density matrix.[11,29,12,33] This work has shown that the internal conversion process induced by vibronic couplings[12] is uniquely marked by an accompanying vibrational energy redistribution and coherent exciton-vibrational dynamics emerges due to non-adiabatic interactions between excited states. Moreover, due to the circular symmetry of CPPs, specific antisymmetric vibrational excitations

modulate the exciton dynamics[48]. Upon photoexcitation, the excess of energy funnels from electronic degrees of freedom to vibrations in the presence of strong vibronic couplings that involve a reduced set of coupled vibrational normal modes. The identification of these so-called active modes represents a valuable knowledge that can be used to manipulate the efficiency of energy dissipation in novel optical-electronic devices[49,50,51,52,53].

Following these earlier studies, the present work explores differences in the optoelectronic properties and photoinduced dynamics of [9]CN and [9]CPP. The more sterically hindered naphthyl units lead to larger dihedral angles between neighboring sites along the backbone. This results in a noticeable modification of photoinduced dynamics for [9]CN as compared to that for [9]CPP as shown by the NEXMD simulations. The paper is organized as follows. Section II provides a methodology overview and computational details. It also includes a description of the analysis of the electronic transition density matrices and normal modes. In Section III we present and discuss our computational results. Finally, Section IV concludes.

II. THEORETICAL METHODOLOGY

A. NEXMD overview

The NEXMD packages[47,46] is a software allowing for efficient and sufficiently accurate direct Non-adiabatic EXcited state Molecular Dynamics simulations, which was specifically developed to simulate photoinduced dynamics of large molecular systems involving multiple coupled electronic excited states. It makes use of the fewest switches surface hopping (FSSH) algorithm[54,55] in combination with "on the fly" analytical calculations of excited-state energies [56,57,58], gradients[59,60], and non-adiabatic coupling terms[47,61,62,63], evaluated within the Collective Electron Oscillator (CEO) approach[64,65,66] at the Configuration Interaction Singles (CIS) level using semiempirical model Hamiltonians such as Austin Model 1 (AM1)[67]. This level of approximation has been previously successfully applied to simulate the photoinduced dynamics of the family of [n]CPPs and other related nanohoops[11,29,12,33].

Briefly, the non-adiabatic dynamics is defined by derivative coupling vectors (**NACR**$_{\alpha\beta}$), which drive the photoexcited electron-vibrational relaxation. These quantities are also calculated analytically[68] within the CEO framework and defined as

$$\mathbf{NACR}_{\alpha\beta} = \left\langle \phi_\alpha(\boldsymbol{r};\boldsymbol{R}(t)) \middle| \nabla_{\boldsymbol{R}} \phi_\beta(\boldsymbol{r};\boldsymbol{R}(t)) \right\rangle \quad (1)$$

Here $\boldsymbol{r}$ and $\boldsymbol{R}(t)$ are the electronic and nuclear vector coordinates, respectively, and $\phi_\alpha(\boldsymbol{r};\boldsymbol{R}(t))$ ($\phi_\beta(\boldsymbol{r};\boldsymbol{R}(t))$) is the α^{th} (β^{th}) adiabatic electronic excited state. The direction of **NACR**$_{\alpha\beta}$ corresponds to the direction of the main nuclei force on the nuclei when non-adiabatic interactions between α^{th} and β^{th} electronic states takes place[50]. Further details about the NEXMD approach, implementation, advantages and testing parameters can be found in our previous work[69,46].

B. Transition density matrix: exciton transient (de)localization, coherences, and intra-ring migration.

During the NEXMD simulations, the intramolecular electronic energy transfer and redistribution can take place through tightly bound Frenkel-type excitons[70,71,72] with electron-hole pairs spatially localized on the same chromophore units or through charge-transfer processes, where electron-hole pairs occupy different units. To delineate between these two cases, here we use real-space analysis of the transition density matrix $\rho^{g\alpha}$ tracking the changes due to transition from ground (g) to excited state[68,64,65]. The elements of this quantity (frequently denoted *electronic normal mode*)[66,73] are defined as $\rho_{nm}^{g\alpha} \equiv \langle \phi_\alpha(\boldsymbol{r};\boldsymbol{R}(t))|c_m^+ c_n|\phi_g(\boldsymbol{r};\boldsymbol{R}(t))\rangle$. Here $c_m^+(c_n)$ represents the creation (annihilation) electronic operator with indices *n* and *m* referring to atomic orbital basis functions.

The exciton transient localization on each X chromophore unit (i.e. phenyl units for [9]CPP and naphthyl units for [9]CN) can be evaluated as

$$\delta_X^\alpha(t) = \sum_{n_A m_A} (\rho_{n_A m_A}^{g\alpha}(t))^2 \qquad (2)$$

Here the index A runs over all atoms localized in the corresponding chromophore unit. The application of the Frenkel exciton model for these systems can be evaluated using the summation of the diagonal blocks

$$\delta_{diagonal}^\alpha(t) = \sum_X \delta_X^\alpha(t) \qquad (3)$$

whereas the summation over off-diagonal elements

$$\delta_{off-diagonal}^\alpha(t) = \sum_{n_A m_B} (\rho_{n_A m_B}^{g\alpha}(t))^2 \qquad (4)$$

with indexes A and B running over the atoms localized on neighbouring chromophore units, is a signature of charge-transfer and electron-hole delocalization between them.

The analysis of the $\rho^{g\alpha}$ matrix can be performed by defining two characteristic sizes (i.e. the diagonal and off-diagonal sizes) of the extent of electron-hole (de)localization among chromophore units. The diagonal size reflects the number of units over which the excitation is spread (i.e., excitonic center of mass delocalization) and it roughly corresponds to the phenyl/naphtyl-unit participation number, PN(t)[74,75], defined as

$$PN(t) = \left[\sum_i^n \left(\delta_X^\alpha(t)\right)^2\right]^{-1} \qquad (5)$$

Values of $PN(t) \approx 1$ indicate a complete localization of the exciton on a single unit, while values of $PN(t) \approx n$ correspond to exciton being fully spread across the *n* units. The off-diagonal size, LC(t)[56], measures the spatial coherence between electrons and holes located at different chromophores.

$$LC(t) = \left[\sum_i^n \left(\delta_X^\alpha(t)\right)^2\right]^{-1} \qquad (6)$$

According to previous works[12], the exciton intra-ring migration is analyzed using the following procedure:

1. $\mathrm{PN}(t_0)$ is evaluated at t_0.
2. The n units of the nanoring are sorted by decreasing values of $\delta_X^{\alpha}(t)$.
3. A vector $v(t_0)$ is constructed, where the elements $v_i(t_0)$, associated to each unit, are
   = 1 if $s_i < \mathrm{PN}(t_0)$
   = 0 otherwise
   Here s_i is the rank of the ith unit according to 2.
4. Steps 1 to 3 are repeated throughout the simulation at every time-step t.

The resulting i^{th} element of vector $v(t)$, averaged over the entire ensemble of the NEXMD simulations, represents the probability of the i^{th} unit to retain a significant contribution to the $\rho^{g\alpha}$ matrix throughout the electronic relaxation process. This allows us to track the exciton intra-ring migration.

C. Excited-State equilibrium normal mode analysis

Excited-state equilibrium normal modes (ES-ENM(S_1))[76] are obtained at the minimum geometry $\mathbf{R}_0$ of the first excited state (S_1). ES-ENM(S_1) are defined by the set of eigenvectors ($\{\mathbf{Q}_i\}$, (i =1,…3N-6, N=being the number # of atoms in the molecule) obtained by diagonalyzing the mass-weighted Hessian matrix **H.** The ES-ENM(S_1) can be expressed as a linear combination of the set $\{\mathbf{q}_i\}$, (i =1,…3N) as

$$\mathbf{Q}_i(t) = \sum_{j=1}^{3N} l_{ji}\mathbf{q}_j(t) \qquad i=1,\ldots,3\text{N-6} \qquad (7)$$

where l_{ji} are the elements of the eigenvector matrix **L**, resulting from the diagonalization of **H**. The corresponding eigenvalues λ_i (i=1, …,*3N-6*) are associated to the normal mode frequencies $\nu_i = \sqrt{\lambda_i}/2\pi$. Any displacement of molecular geometry, such as $\mathbf{NACR}_{12}$ vector , can be expanded in ES-ENM(S_i) basis:

$$\mathbf{NACR}_{12} = \sum_{i=1}^{3N-6} c_i\mathbf{Q}_i \quad (\alpha=1,2) \qquad (8)$$

with $c_i = \mathbf{Q}_i \cdot \mathbf{NACR}_{12}$ (9)

We can further define the participation number PN of these projections as

$$PN_{\mathbf{NACR}} = \left(\sum_{i=1}^{3N-6}\left(c_i^{\alpha}\right)^4\right)^{-1} \qquad (10)$$

According to the virial theorem, the total vibrational energy $E_i(t)$ associated with a given ES-ENM(S_1) can be calculated as twice the kinetic energy $K_i(t)$, i.e. $E_i(t) = 2K_i(t)$, with

$$K_i(t) = \left(\dot{\mathbf{Q}}_i(t)\right)^2 \qquad (11)$$

and the ES-ENM(S_1) momenta are calculated as

$$\dot{\mathbf{Q}}_i(t) = \sum_{j=1}^{3N} l_{ji}\dot{\mathbf{q}}_j(t) \qquad i=1,\ldots,3N\text{-}6 \qquad (12)$$

While NEXMD simulations are performed in the *space-fixed* Cartesian coordinates, linear transformations shown in **eq. 8** and **10** express $\{\mathbf{Q}_i,\dot{\mathbf{Q}}_i\}$ on the basis of mass-weighted Cartesian displacements $\{\mathbf{q}_i,\dot{\mathbf{q}}_i\}$ defined in the *body-fixed* Cartesian reference frame with the origin in its center of mass and its inertial axis coincident with the original Cartesian *x,y,z* axis. Therefore, in order to apply them, coordinates and velocities obtained from the NEXMD simulations must be erstwhile translated and rotated from the *space-fixed* to the *body-fixed* reference frame. More details about the calculations of ES-ENM(S_1) can be found elsewhere[76].

D. Computational details

The NEXMD simulations were conducted on [9]CPP and [9]CN molecules at constant energy. The initial positions and momenta of the nuclei were obtained from 1000 snapshots, equispaced on time, collected from a 4 ns equilibrated ground state (S_0) molecular dynamics simulation, with the system equilibrated at room (300K) temperature using the Langevin thermostat and a friction coefficient of 20 ps^{-1}. For each NEXMD simulation, the initial excited state is then selected according to a Frank-Condon window given by $g_\alpha(\boldsymbol{r},\boldsymbol{R}) = \exp\left[-T^2(E_{laser}-\Omega_\alpha)^2\right]$ where E_{laser}, expressed in units of fs^{-1} as well as Ω_α, represents the energy of a laser centred at 2.8 eV and 3.1 eV that corresponds to the maximum of the calculated absorption spectrum for [9]CN and [9]CPP respectively. A Gaussian laser pulse, $f(t) = \exp(-t^2/2T^2)$, with T=42.5 fs, corresponding to a FWHM (Full Width at Half Maximum) of 100 fs, has been used. For each NEXMD simulation, the relative values of $g_\alpha(\boldsymbol{r},\boldsymbol{R})$, weighted by the oscillator strengths of each α state, have been used to select its initial excited state.

Ten electronic states and their corresponding non-adiabatic couplings were included in the simulations. Classical time steps of 0.5 fs and 0.1 fs have been used for nuclei propagation in ground-state and NEXMD simulations respectively. Besides, a quantum time step of 0.025 fs has been used to propagate the electronic degrees of freedom during the NEXMD simulations. In order to identify and deal with trivial unavoided crossings, the quantum time step was further reduced by a factor of 40 in the vicinity of such crossings[77].

III. RESULTS AND DISCUSSION

We have performed a comparative study of the photoexcitation and subsequent energy relaxation and redistribution in extended π-conjugated carbon nanorings composed of nine naphthyl units ([9]CN) and nine phenyl units ([9]CPP), shown in **Figure 1(a)**t. [9]CN represents the first synthetized π-extended carbon nanoring[36]. Here our simulations attempt to analyse how the replacement of phenyl with acene unit (while preserving the overall centrosymmetric nature of the system) affects the structural, dynamics and optical properties of a carbon nanoring.

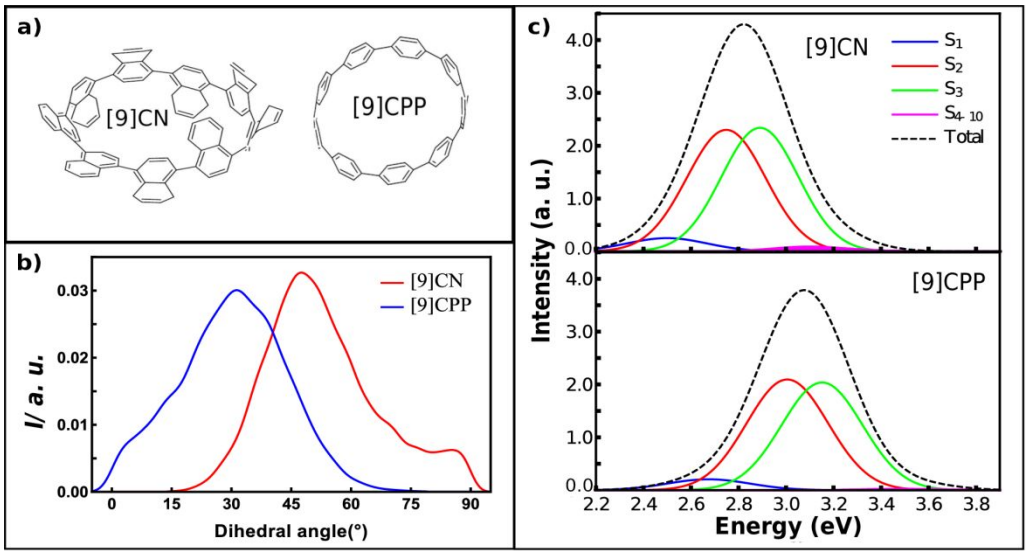

Figure 1. (a) Schematic representation of [9]CN, and [9]CPP molecules; (b) Dihedral angle distributions computed via ground-state dynamics simulations in thermal equilibrium at 300 K; (c) Simulated absorption spectra of molecules along with separated contributions of different excited states.

Figure 1(b) shows the distribution of the dihedral angles between the neighbouring units for [9]CN, and [9]CPP molecules obtained from the equilibrated molecular dynamics simulation at room temperature (see **Section II.D**). The average dihedral angle (~50°) between neighboring units for [9]CN is larger than the corresponding value of ~30° for [9]CPP due to enhanced steric hindrance in the former system. Besides, as [9]CN and [9]CPP are odd-numbered nanorings, the lowest-energy conformation with all the acene rings alternately staggered is not possible[10,8,78]. Therefore, they are structurally frustrated[11]. This is observed in **Figure 1(b)** where the shoulder at ~10-15° in the distribution of dihedral angles of [9]CPP corresponds to one phenyl unit that results aligned perpendicular to the plane of the nanoring. In contrast, the corresponding distribution for [9]CN shows a shoulder at ~85-90° that indicates one naphthyl unit is aligned almost parallel to the nanoring plane. These results confirm that the localized frustrated structures, previously observed for the optimized geometry[36], also persist at room temperature.

The average dihedral angles increase with the size of CPPs due to relaxation of the backbone strain. In contrast, the increase of the average dihedral angle observed in [9]CN compared to [9]CPP should be associated to the more sterically demanding naphthyl units as against phenyl units. The expected blue shift in the absorption spectra of [*n*]CPPs with the increase of the torsions between phenyl units while increasing *n,* is compensated by a red shift caused by a larger π-conjugation length. As a result, the absorption maxima of [*n*]CPPs are independent of *n*. This is not the case for [9]CN for which the π-extension of the naphthyl unis leads to a red shift in the absorption spectra in comparison with that of [9]CPP. This is shown in **Figure 1(c)** where the absorption spectra of [9]CN and [9]CPP are displayed. In a good agreement with experiment[36], the absorption spectrum of [9]CN is red shift by ~0.3 eV with respect to that of [9]CPP. In both cases, the main contribution to the main absorption peak originates from S_2 and S_3 excited states that are strongly optically allowed due to the circular structure of the molecule. The S_1 state is optically forbidden in such geometries due to symmetry[11].

Nevertheless, the symmetry breaking due to thermal fluctuations results in non-vanishing oscillator strengths for S_1 state in both molecules.

The simulated ultrafast electronic energy relaxation for [9]CN and [9]CPP is displayed in **Figure 2** as the evolution in time of the average population of each electronic excited state that participate in the process. We can observe that the internal conversion process is quite similar in both systems. Here following photoexcitation at the maximum of absorption band (see **Figure 1c**), the initial state is roughly equally distributed between S_2 and S_3 states. After that, an efficient ultrafast sequential $S_3 \rightarrow S_2 \rightarrow S_1$ and $S_2 \rightarrow S_1$ processes take place. Only 8% and 2% of all trajectories, for [9]CN and [9]CPP, respectively, have experienced a direct $S_3 \rightarrow S_1$ energy transfer. Previous results have shown that, at room temperature, the internal conversion process of [*n*]CPPs barely depends on *n*, and at about 250 fs the lowest S_1 state is becoming completely populated. **Figure 2** indicates that this process is also weakly affected by replacement of phenyl with acene units that compose the nanoring, and the relaxation timescales are very similar in [9]CN and [9]CPP.

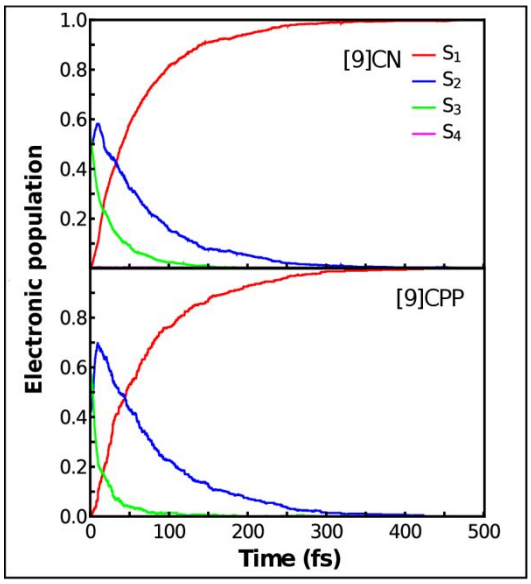

Figure 2. Average population on each electronic surface as a function of time obtained from the time-dependent fraction of trajectories in each state during NEXMD simulations of [9]CN (upper panel) and [9]CPP (lower panel).

The intramolecular electronic energy redistribution that takes place during internal conversion has been monitored through variation of $\delta^{\alpha}_{diagonal}(t)$, $\delta^{\alpha}_{off-diagonal}(t)$, PN(t), and LC(t) variables (**eqs. 3-5**) plotted in **Figure 3**. The time-evolution of $\delta^{\alpha}_{diagonal}(t)$ and, $\delta^{\alpha}_{off-diagonal}(t)$, shown in **Figures 3(a, b)**, indicates the pre-dominant the Frenkel exciton character of the electronic excitation during the internal conversion process for both systems. Our definition of $\delta^{\alpha}_{off-diagonal}(t)$ (see **eq. 4**) involves only the summation over atoms localized on neighbouring chromophore units. Therefore, values of $\delta^{\alpha}_{diagonal}(t)$ + $\delta^{\alpha}_{off-diagonal}(t)$ is approximately equal to 1 throughout the simulations indicate that electron-hole pairs are mostly spatially localized on the same chromophore unit or occupy the neighboring units. After photoexcitation, and while the internal conversion

process evolves in time, $\delta^{\alpha}_{\text{diagonal}}(t)$ decreases and $\delta^{\alpha}_{\text{off-diagonal}}(t)$ increases. That is, the non-adiabatic electronic excited state dynamics leads the molecular system to explore regions of the potential energy surface with stronger interactions (and thus electronic delocalization) between neighbouring chromophore units. As intuitively expected, the interaction between phenyl units in [9]CPP is larger than that between naphthyl units in [9]CN.

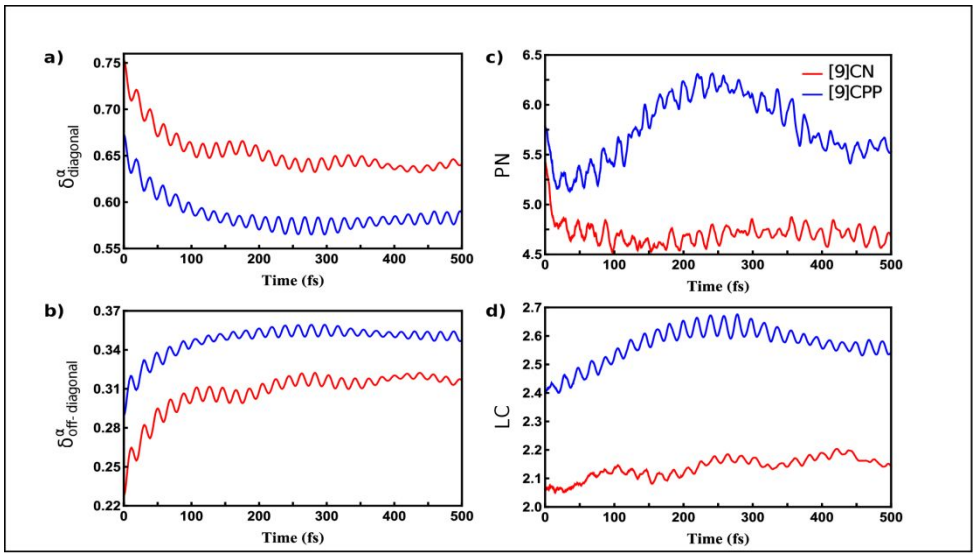

Figure 3. The evolution in time of the diagonal $\delta^{\alpha}_{\text{diagonal}}$ (a) and off-diagonal $\delta^{\alpha}_{\text{off-diagonal}}$ (b) sums **(eqs. 3** and **4**) of the transition density matrix, phenyl/naphtyl-unit participation number PN (c), that measures the number of units over which the excitation is spread (**eq. 5**), and LC(d), that measures the degree of separation between electrons and holes at different chromophores (**eq. 6**).

Figure 3(c) shows the evolution of PN (see **eq. 5**) during the NEXMD simulations. PN is always significantly lower than 9 due to structural disorder introduced by thermal fluctuations. After an initial ultrafast contraction of $\rho^{g\alpha}$, the exciton remains dynamically self-trapped within ≈4-6 units. While the exciton of [9]CN remains steadily confined within 4-5 units throughout the rest of our simulations, the exciton of [9]CPP experiences a transient delocalization to up to 6 units. In general, **Figure 3(c and d)** shows that the exciton in [9]CPP is more diagonally delocalized with larger spatial electron-hole separation between phenyl units (i.e. we observe consistently larger PN(t) and LC(t) values) than that in [9]CN. This is also seen in **Figure 4,** which displays the entire two-dimensional plots of the transition density matrix $\rho^{g\alpha}$ for the current state, on the basis of the atomic orbitals of the chromophore units, evaluated at several points in time after photoexcitation for a typical NEXMD trajectory obtained for [9]CN and [9]CPP. The amplitudes of the off-diagonal quadrants indicating charge-transfer character between units, remain an order of magnitude smaller than the amplitudes of the diagonal blocks. Moreover, $\rho^{g\alpha}_{\text{nm}} \approx \rho^{g\alpha}_{\text{mn}}$ means there is no directional charge-transfer. Notably, for all cases, it is noticeable that the exciton migrates along the molecular backbone with time.

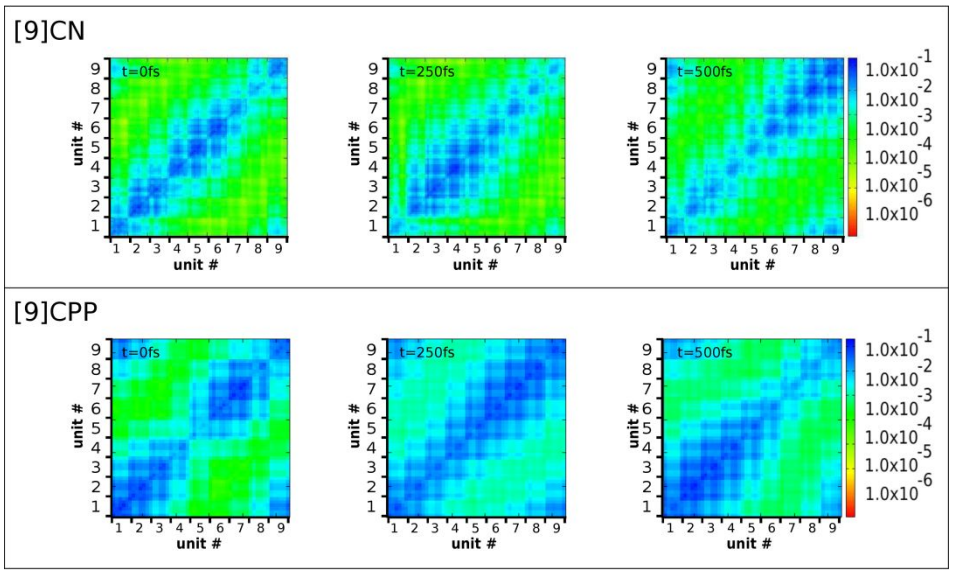

Figure 4. Two-dimensional plots of transition density matrix elements for the current state, on the basis of chromophore unit atomic orbitals, at t = 0 fs, t=250fs and t=500fs for a representative NEXMD trajectory. The x and y axes denote spatial positioning of an electron and a hole in respective atomic orbitals for chromophore units ordered along the molecular backbone. The color coding is shown on the right hand side.

The transient increase of the exciton delocalization in [9]CPP dynamics shown in **Figures 3(c)** and **4** is concomitant to the transient planarization of the nanoring experienced by [9]CPP as depicted in **Figure 5**. Despite the fact that [9]CN also experiences similar planarization, the electronic effect is less evident in this molecule compared to [9]CPP. Excited state planarization have been previously reported in multiple experimental and theoretical works and can be considered as a general phenomenon of dynamics of π-π* electronic excitations in conjugated chromophores[79,80,81,82,83,84,12,33]. Here we observe that conformational disorder at room temperature leads to wider angular distributions reflecting faster phenyl rotations than the slower naphthyl ones. That is, relatively rapid rotation of phenyl units leads to a pronounced transient planarization and exciton delocalization, as shown by higher PN(t) values for [9]CPP compared to that for [9]CN.

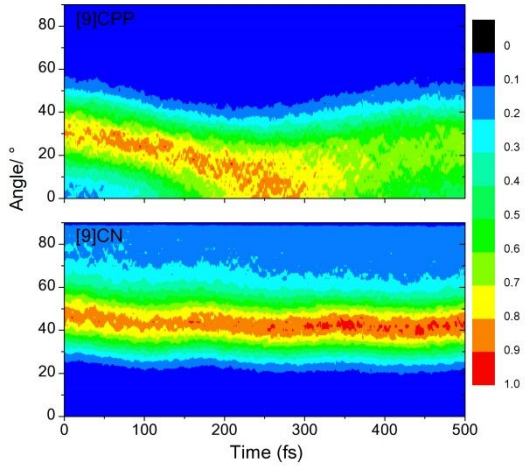

Figure 5. Time evolution of the probability density of the dihedral angles between neighboring phenyl/naphthyl units during NEXMD simulations of [9]CPP (upper panel) and [9]CN (lower panel) respectively.

Such enhanced conformational dynamics in [9]CPP leads to a more rapid exciton intra-ring migration on sub 100fs timescale compared to that in [9]CN. **Figure 6** displays the probability of each phenyl/naphthyl unit to retain a significant portion of $\rho_{nm}^{g\alpha}$ (t) that has been calculated following the procedure described in **Section 2B**. While the internal conversion process leads to a similar probability for all units in both nanorings at the long timescales, the process saturates faster in [9]CPP compared to that in [9]CN. Nevertheless, a transient collective increase of probability for all units is observed for [9]CPP at ~250 fs. This behavior can be associated with the transient exciton delocalization shown in Figure 3(c) and not observed for [9]CN. Finally, the conformational rearrangements of chromophore units lead to a completely random final exciton localization for both system with equivalent ~ 0.5 probabilty for all units no matter the initial exciton localization.

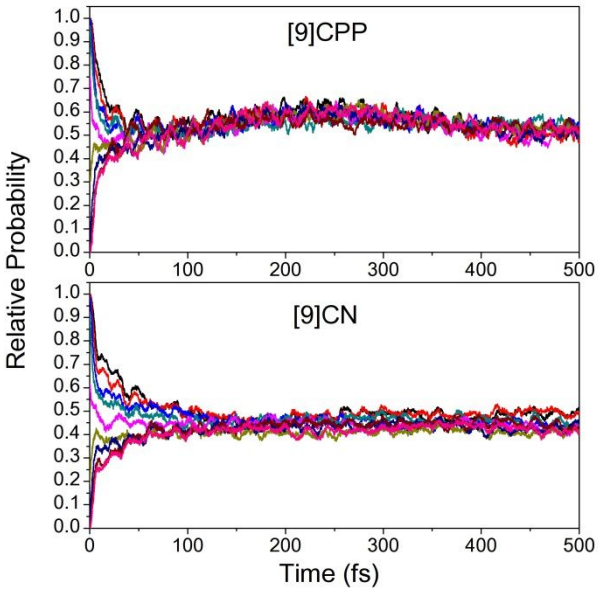

Figure 6. Variation in time of the relative probability of each phenyl/naphthyl unit to retain a portion of the total electronic transition density during the NEXMD simulations of [9]CPP (upper panel) and [9]CN (lower panel) respectively.

After photoexcitation, electronic energy relaxation and redistribution are controlled by vibronic couplings, involving the so-called active vibrational normal modes. This reduced set of coupled nuclei motions is commonly identified by their projections along the non-adiabatic coupling vector $\mathbf{NACR}_{\alpha\beta}$ (see **eq. 1**). The direction of $\mathbf{NACR}_{\alpha\beta}$ represents the direction of the force acting on the nuclei during the $S_\alpha \rightarrow S_\beta$ transition (the so-called Pechukas force)[50]. The excess of energy that funnels from electronic degrees of freedom to vibrations takes place in the direction of $\mathbf{NACR}_{\alpha\beta}$. This energy funneling impacts the efficiency of energy dissipation and final electronic state

proceeding the emission event. Herein, we have performed a further inspection of **NACR**$_{12}$ by projecting it onto the ES-ENM(S_1) basis set according to **eqs 8** and **9**.

Following **eq. 10**, $PN_{\mathbf{NACR}}$ represents the number of ES-ENMs(S_1) that contribute to **NACR**$_{12}$. Values of $PN_{\mathbf{NACR}} \approx 3N\text{-}6$ indicate that the direction of **NACR**$_{12}$ involves the participation of all ES-ENM(S_1) variables, whereas $PN_{\mathbf{NACR}} \approx 1$ indicates that it corresponds to a unique ES-ENM(S_1) mode. **Figure** 7 shows the distribution of values of $PN_{\mathbf{NACR}}$, at the moment of effective $S_2 \rightarrow S_1$ transition, for each NEXMD simulation. While the direction of **NACR**$_{12}$ involves only ~ 4 ES-ENMs(S_1) for [9]CN (modes at 1748.4 cm^{-1}, 1753.9 cm^{-1}, 1576.6 cm^{-1} and 1578.3 cm^{-1}), it is spread on an average of ~ 10 ES-ENMs(S_1) for [9]CPP (modes at 1666.8 cm^{-1}, 1666.8 cm^{-1}, 1776.7 cm^{-1} and 1776.7 cm^{-1} being the dominant contributions). That is, the the energy dissipation is more efficient in [9]CN. Despite that, for both molecules, the set of modes that overlap the most with **NACR**$_{12}$ comprises modes within two ranges of frequencies: ~1700-1780 cm^{-1} and ~ 1550-1600 cm^{-1} for [9]CN and ~1750-1800 cm^{-1} and ~ 1650-1700 cm^{-1} for [9]CPP. That is, the range of frequencies for the active modes is quite close for both nanorings. This can be seen in **Figure 8** that shows the distribution of the projection of **NACR**$_{12}$ onto each ES-ENM(S_1). Two modes for each molecule, representing the main contributions to **NACR**$_{12}$ direction, are also depicted. They correspond to equivalent motions associated to doubly-degenerate in-plane E_{2g} vibrations of benzene (1763 cm^{-1}) but involving different phenyl units on the ring. This is also the case for modes related to the minor peaks (see **Figure S1**), that can be associated to collective motions in which each phenyl unit displays equivalent motions to the doubly degenerate in-plane E_{1u} normal modes of benzene (1658cm^{-1}). That is, the circular symmetry of CPPs leads to the excitation of pairs of specific degenerate antisymmetric vibrational modes that modulate the exciton dynamics[12,48], ultimately leading to a final exciton self-trapping with random localizations for both systems.

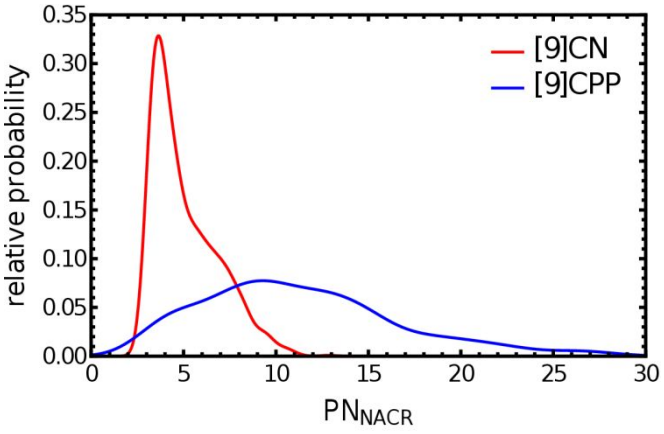

Figure 7. Distribution of $PN_{\mathbf{NACR}}$ values, representing the number of ES-ENMs(S_1) that contribute to **NACR**$_{12}$ at the moment of effective $S_2 \rightarrow S_1$ transition for NEXMD simulation of [9]CPP and [9]CN.

.

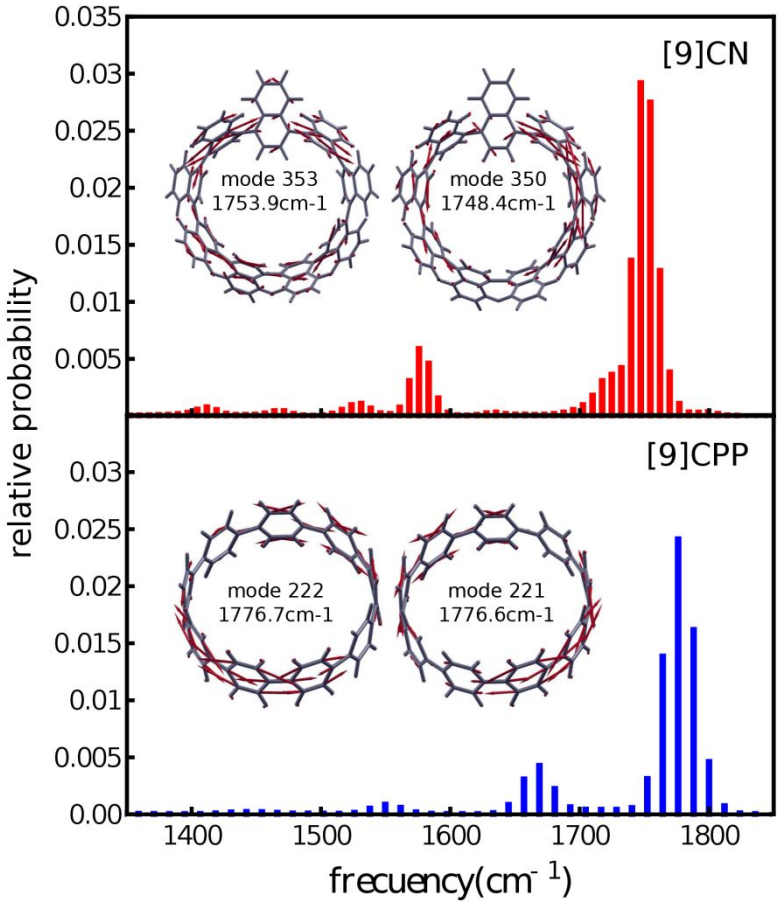

Figure 8. Distribution of the projection of **NACR**$_{12}$ at the moment of effective $S_2 \rightarrow S_1$ transition for each NEXMD simulation onto the basis of ES-ENM(S_1). Modes that represent the main contributions to **NACR**$_{12}$ direction are shown.

Vibrations associated to the major and minor peaks of **Figure 8** are responsible of the fast oscillations in the localization/delocalization of the exciton, with periods of roughly ~18-22 fs as shown in **Figure 3.** These fast oscillations, persisting even at room temperature, are a consequence of the vibronic couplings induced in the direction of these set of normal modes and they suggest the formation of 'coherent phonons', a phenomena that has been previously reported, for example, in carbon nanotubes[85,86,87].

The intramolecular vibrational energy flow, accompanying the electronic energy relaxation, can be monitored by analyzing the average vibrational energy $E_i(t)$ throughout the NEXMD simulations. **Figure 9** shows the time-evolution of the average $E_i(t)$ for different intermediate- and high-frequency ES-ENMs(S_1). We observe that a reduced set of active normal modes experiences a transiently accumulation of $E_i(t)$ during the first ~250 fs of dynamics after photoexcitation. The rest of the modes remains with average values of $E_i(t)$ close to their corresponding thermal equilibrium value (kT = 0.026 eV). The coupled active modes mostly correspond to those motions previously identified as overlapping with **NACR**$_{12}$. In fact, these two set of modes perfectly match for [9]CPP. Nevertheless, the higher density of vibrational states of [9]CN introduces a higher degree of mixing between modes that are close in frequency at room temperature, washing out their individual identities defined at the minimum of S_1 state.

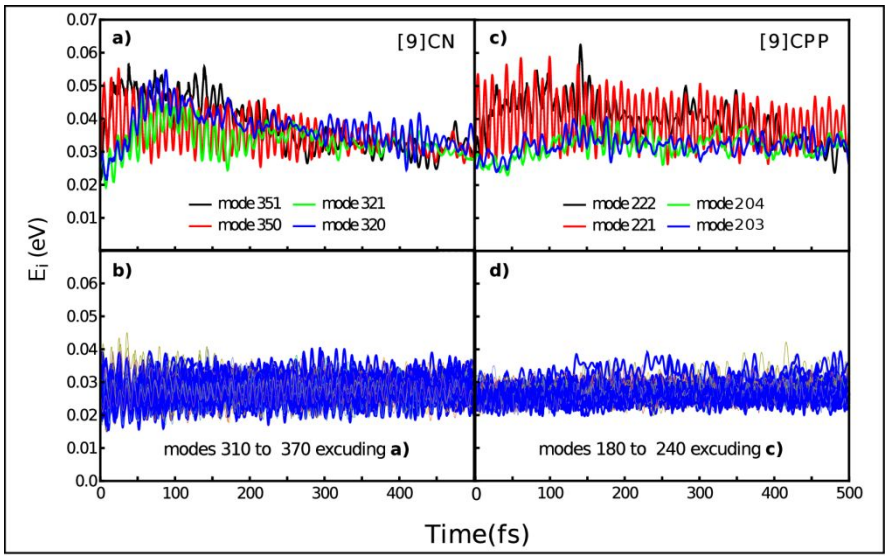

Figure 9. Time evolution of the total energy of trajectories along (a) active normal modes, and (b) other normal modes excluding those plotted in part a for [9]CN, (c) active normal modes, and (d) all the normal modes excluding those plotted in part c for [9]CPP.

The identification of a reduced subset of active modes that participates of the internal conversion process, while the rest of the modes serve as a bath of coupled harmonic oscillators into which the excess of energy is dissipated, points to the possibility to carry out simulations of the photoinduced non-adiabatic dynamics in which only this subset of active modes is considered explicitly. The influence of bath modes could be incorporated via a spectral density (e.g., using its connection to the memory kernel in the generalized Langevin equation), as it is customary in system-bath dynamics simulations. Within this approach, NEXMD simulations can initially contribute to identify active normal modes, to compute the spectral density, and to check the validity of underlying assumptions such as the linearity of the system-bath coupling or the adequacy of using the same spectral density for all the states in the populated electronic manifold. Subsequently, accurate simulations of the photoinduced dynamics along the active modes could be undertaken. Such a two-step simulation procedure is very appealing in situations in which the separation between the system and the bath makes quantum mechanical simulations (of the reduced-dimensionality system) computationally affordable. Owing to middle- to high-frequency character of the normal modes, which participate actively in the internal conversion in 9-phenyl and 9-naphthyl carbon nanorings, a moderate influence of their zero-point energy on the exciton relaxation pathway could be expected. Work in this direction is currently underway.

IV. CONCLUSIONS

We have performed a comparative study of the structure, optical properties, non-adiabatic excited state dynamics and electron-vibrational relaxation of two carbon nanorings composed of nine phenyl ([9]CPP) and nine naphthyl ([9]CN) units using the NEXMD software. The computational results are analyzed with transition density matrices enabling the assessment of time-dependent electronic properties and excited

state vibrational normal modes reflecting conformational dynamics. The more sterically distorted and slow moving naphthyl units lead to average higher dihedral angles between the neighboring units and less efficient structural planarization in the excited states that impacts the exciton self-trapping during the internal conversion process. In general, the exciton in [9]CPP is more delocalized across several structural repeat units compared to that in [9]CN. While the exciton intra-ring migration is faster in [9]CPP than that in [9]CN, structural rearrangements of chromophore units ultimately lead to a random final spatial exciton localization for both systems.

After photoexcitation, electronic energy relaxation and redistribution take place through specific sets of active normal modes strongly coupled to the electronic degrees of freedom. Either for [9]CN or [9]CPP molecule, these active normal modes correspond to in-plane vibrations within similar narrow ranges of middle- to high-frequencies. This common feature of the vibrations associated to the electronic energy transfer process, is responsible for overall similar internal conversion processes observed in both systems. Our results provide detailed information on how features of vibrations such as their frequencies and collective character, have a direct impact on the exciton redistribution during the internal conversion, self-trapping, and intra-ring migration. Computational predictions on electronic energy dissipation and ability of these active modes to absorb an excess of electronic energy after photoexcitation deliver a valuable knowledge that can be used in experiment to manipulate the efficiency of energy dissipation in emerging optical-electronic devices.

Acknowledgement

This work was performed in part at the Center for Nonlinear Studies (CNLS) and the Center for Integrated Nanotechnology (CINT), a U.S. Department of Energy and Office of Basic Energy Sciences user facility. We acknowledge support from the Los Alamos National Laboratory (LANL) Directed Research and Development funds (LDRD). This research used resources provided by the LANL Institutional Computing Program. S.F.A. acknowledges support of CONICET, UNQ and ANPCyT (PICT-2018-02360).

References

1 P. Evans and R. Jasti, Molecular Belts, *Top. Curr. Chem.*, 2014, **349**, 249–290.
2 H. Omachi, Y. Segawa and K. Itami, Synthesis and Racemization Process of Chiral Carbon Nanorings: A Step toward the Chemical Synthesis of Chiral Carbon Nanotubes, *Org. Lett.*, 2011, **13**, 2480.
3 R. Jasti and C. Bertozzi, Progress and challenges for the bottom-up synthesis of carbon nanotubes with discrete chirality, *Chem. Phys. Lett.*, 2010, **494**, 1.
4 G. Bodwell, Carbon nanotubes: Growth potential, *Nat. Nanotechnol.*, 2010, **5**, 103.
5 M. Iyoda, J. Yamakawa and M. J. Rahman, Conjugated Macrocycles: Concepts and Applications, *Angew. Chem., Int. Ed.*, 2011, **50**, 10522.
6 T. Kawase and H. Kurata, Ball-, Bowl-, and Belt-Shaped Conjugated Systems and Their Complexing Abilities: Exploration of the Concave−Convex π−π Interaction, *Chem. Rev.*, 2006, **106**, 5250.
7 B. Steinberg and L. Scott, New Strategies for Synthesizing Short Sections of Carbon Nanotubes, *Angew. Chem., Int. Ed.*, 2009, **48**, 5400.
8 S. Lewis, Cycloparaphenylenes and related nanohoops, *Chem. Soc. Rev.*, 2015, **44**, 2221–2304.

9 Y. Segawa, S. Miyamoto, H. Omachi, S. Matsuura, P. Senel, T. Sasamori, N. Tokitoh and K. Itami, Concise synthesis and crystal structure of [12]CPP, *Angew. Chem., Int. Ed.*, 2011, **50**, 3244.

10 Y. Segawa, A. Fukazawa, S. Matsuura, H. Omachi, S. Yamaguchi, S. Irle and K. Itami, Combined experimental and theoretical studies on the photophysical properties of cycloparaphenylenes, *Org. Biomol. Chem.*, 2012, **10**, 5979–5984.

11 L. Adamska, I. Nayyar, H. Chen, A. Swan, N. Oldani, S. Fernandez-Alberti, M. Golder, R. Jasti, S. Doorn and S. Tretiak, Self-trapping of excitons, violation of Condon approximation and efficient fluorescence in conjugated cycloparaphenylenes, *Nano Lett.*, 2014, **14**, 6539–6546.

12 N. Oldani, S. K. Doorn, S. Tretiak and S. Fernandez-Alberti, Photoinduced dynamics in cycloparaphenylenes: Planarization, electron-phonon coupling, localization and intra-ring migration of the electronic excitation, *Phys. Chem. Chem. Phys.*, 2017, **19**, 30914–30924.

13 E. J. Leonhardt and R. Jasti, Emerging applications of carbon nanohoops, *Nat. Rev. Chem.*, 2019, **3**, 672–686.

14 J. M. . Van Raden, B. M. . White, L. N. . Zakharov and R. Jasti, Nanohoop rotaxanes via active metal template syntheses and their potential in sensing applications., *Angew. Chem. Int. Ed.*, 2019, **58**, 7341–7345.

15 B. White, Y. Zhao, T. Kawashima, B. Branchaud, M. Pluth and R. Jasti, Expanding the chemical space of biocompatible fluorophores: nanohoops in cells., *ACS Cent. Sci.*, 2018, **4**, 1173–1178.

16 N. Ozaki, H. Sakamoto, T. Nishihara, T. Fujimori, Y. Hijikata, R. Kimura, S. Irle and K. Itami, Electrically activated conductivity and white light emission of a hydrocarbon nanoring–iodine assembly., *Angew. Chem. Int. Ed.*, 2017, **56**, 11196–11202.

17 P. Della Sala, N. Buccheri, A. Sanzone, M. Sassi, P. Neri, C. Talotta, A. Rocco, V. Pinchetti, L. Beverina, S. Brovelli and C. Gaeta, First demonstration of the use of very large Stokes shift cycloparaphenylenes as promising organic luminophores for transparent luminescent solar concentrators., *Chem. Commun.*, 2019, **55**, 3160–3163.

18 Y. Segawa, P. Senel, S. Matsuura, H. Omachi and K. Itami, Concise synthesis and crystal structure of [9]CPP, *Chem. Lett.*, 2011, **40**, 423.

19 T. Iwamoto, Y. Watanabe, T. Sadahiro, T. Haino and S. Yamago, Size-selective encapsulation of C60 by [10]cycloparaphenylene: Formation of the shortest fullerene-peapod, *Angew. Chemie - Int. Ed.*, 2011, **50**, 8342–8344.

20 C. . Reese and Z. Bao, Organic single- crystal field- effect transistors., *Mater. Today*, 2007, **10**, 20–27.

21 Y. Nakagawa, R. Sekiguchi, J. Kawakami and S. Ito, Preparation of a large-sized highly flexible carbon nanohoop, *Org. Biomol. Chem.*, 2019, **17**, 6843–6853.

22 A. Yagi, G. Venkataramana, Y. Segawa and K. Itami, Synthesis and properties of cycloparaphenylene2,7-pyrenylene: a pyrene-containing carbon nanoring, *Chem. Commun.*, 2014, **50**, 957–959.

23 T. Iwamoto, E. Kayahara, N. Yasuda, T. Suzuki and S. Yamago, Synthesis, Characterization, and Properties of [4]Cyclo-2,7-pyrenylene: Effects of Cyclic Structure on the Electronic Properties of Pyrene Oligomers, *Angew. Chem., Int. Ed.*, 2014, **53**, 6430–6434.

24 R. Franklin-Mergarejo, T. Nelson, S. Tretiak and S. Fernandez-alberti, Phonon bottleneck and long-lived excited states in p-conjugated pyrene hoop, *Phys. Chem. Chem. Phys.*, 2017, **19**, 9478–9484.

25 J. Xia, J. Bacon and R. Jasti, Gram-Scale Synthesis and Crystal Structures of [8]- and [10]CPP, and the Solid-State Structure of C60@[10]CPP, *Chem. Sci.*, 2012, **3**, 3018.

26 T. Iwamoto, Y. Watanabe, H. Takaya, T. Haino, N. Yasuda and S. Yamago, Size- and orientation- selective encapsulation of C70 by cycloparaphenylenes., *Chem. Eur. J.*, 2013, **19**, 14061–14068.

27 T. Iwamoto, Z. Slanina, N. Mizorogi, J. Guo, T. Akasaka, S. Nagase, H. Takaya, N. Yasuda, T. Kato and S. Yamago, Partial charge transfer in the shortest possible metallofullerene peapod, La@C82c[11]cycloparaphenylene, *Chem. - A Eur. J.*, 2014, **20**, 14403–14409.

28 H. Ueno, T. Nishihara, Y. Segawa and K. Itami, Cycloparaphenylene- based ionic donor–acceptor supramolecule: isolation and characterization of Li+@ C60⊂[10]CPP., *Angew. Chem. Int. Ed.*, 2015, **54**, 3707–3711.

29 R. Franklin-Mergarejo, D. O. Alvarez, S. Tretiak and S. Fernandez-Alberti, Carbon nanorings with inserted acenes: Breaking symmetry in excited state dynamics, *Sci. Rep.*, 2016, **6**, 31253.

30 B. M. Wong and J. W. Lee, Anomalous Optoelectronic Properties of Chiral Carbon Nanorings…and One Ring to Rule Them All(23), *J. Phys. Chem. Lett.*, 2011, **2**, 2702–2706.

31 K. Itami, Toward controlled synthesis of carbon nanotubes and graphenes, *Pure Appl. Chem.*, 2012, **84**, 907–916.

32 P. Li, T. Sisto, E. Darzi and R. Jasti, The Effects of Cyclic Conjugation and Bending on the Optoelectronic Properties of Paraphenylenes, *Org. Lett.*, 2013, **16**, 182–185.

33 B. Rodriguez-Hernandez, D. Ondarse-Alvarez, N. Oldani, A. Martinez-Mesa, L. Uranga-Piña, S. Tretiak and S. Fernandez-Alberti, Modification of Optical Properties and Excited-State Dynamics by Linearizing Cyclic Paraphenylene Chromophores, *J. Phys. Chem. C*, 2018, **122**, 16639−16648.

34 T. Sisto, X. Tian and R. Jasti, Synthesis of Tetraphenyl-Substituted [12]Cycloparaphenylene: Toward a Rationally Designed Ultrashort Carbon Nanotube, *J. Org. Chem.*, 2012, **77**, 5857.

35 T. C. Lovell, C. E. Colwell, N. Zakharov and R. Jasti, Symmetry breaking and the turn-on fluorescence of small, highly strained carbon nanohoops, *Chem. Sci.*, 2019, **10**, 3786–3790.

36 A. Yagi, Y. Segawa and K. Itami, Synthesis and Properties of [9]Cyclo-1,4-naphthylene: A π-Extended Carbon Nanoring, *J. Am. Chem. Soc.*, 2012, **134**, 2962–2965.

37 S. Canola, C. Graham, A. Pérez-Jiménez, J.-C. Sancho-García and F. Negri, Charge transport parameters for carbon based nanohoops and donor–acceptor derivatives, *Phys. Chem. Chem. Phys.*, 2019, **21**, 2057–2068.

38 B. Smith and A. Akimov, Modeling nonadiabatic dynamics in condensed matter materials: some recent advances and applications, *J. Phys. Condens. Matter*, 2019, **32**, 073001.

39 L. Stojanovic, S. G. Aziz, R. H. Hilal, F. Plasser, T. A. Niehaus and M. Barbatti, Nonadiabatic Dynamics of Cycloparaphenylenes with TD-DFTB Surface Hopping, *J. Chem. Theor. Comput.*, 2017, **13**, 5946–5860.

40 P. Kim, K. H. Park, W. Kim, T. Tamachi, M. Iyoda and D. Kim, Relationship between Dynamic Planarization Processes and Exciton Delocalization in Cyclic Oligothiophenes, *J. Phys. Chem. Lett.*, 2015, **6**, 451–456.

41 M. R. Talipov, R. Jasti and R. Rathore, A Circle Has No End: Role of Cyclic

Topology and Accompanying Structural Reorganization on the Hole Distribution in Cyclic and Linear Poly-p-phenylene Molecular Wires, *J. Am. Chem. Soc.*, 2015, **137**, 14999–15006.

42 K. H. Park, P. Kim, W. Kim, H. Shimizu, M. Han, E. Sim, M. Iyoda and D. Kim, Excited-State Dynamic Planarization of Cyclic Oligothiophenes in the Vicinity of a Ring-to-Linear Excitonic Behavioral Turning Point Angewandte, *Angew. Chem. Int. Ed.*, 2015, **54**, 12711–12715.

43 K. H. Park, W. Kim, J. Yang and D. Kim, Excited-state structural relaxation and exciton delocalization dynamics in linear and cyclic p-conjugated oligothiophenes, *Chem Cent. Soc. Rev.*, 2018, **47**, 4279–4294.

44 V. Reddy and S. Irle, An indirect intersystem crossing ($S\,1 \rightarrow T\,3$ / $T\,2 \rightarrow T\,1$) promoted by Jahn-Teller effect in cycloparaphenylenes, *J. Chem. Theor. Comput.*, 2017, **13**, 4944–4949.

45 T. Nelson, S. Fernandez-Alberti, A. E. Roitberg and S. Tretiak, Electronic Delocalization, Vibrational Dynamics, and Energy Transfer in Organic Chromophores, *J. Phys. Chem. Lett.*, 2017, **8**, 3020−3031.

46 A. Sifain, J. Bjorgaard, T. Nelson, B. Nebgen, A. White, B. Gifford, D. Gao, O. Prezhdo, S. Fernandez-Alberti, A. Roitberg and S. Tretiak, Photoexcited Nonadiabatic Dynamics of Solvated Push-Pull π-Conjugated Oligomers with the NEXMD Software, *J. Chem. Theory Comput.*, 2018, **14**, 3955–3966.

47 T. Nelson, S. Fernandez-Alberti, A. E. Roitberg and S. Tretiak, Nonadiabatic Excited State Molecular Dynamics: Modeling Photophysics in Organic Conjugated Materials, *Acc. Chem. Res.*, 2014, **47**, 1155–1164.

48 T. Nelson, D. Ondarse-Alvarez, N. Oldani, B. Rodriguez-Hernandez, L. Alfonso-Hernandez, J. Galindo, V. Kleiman, S. Fernandez-Alberti, A. Roitberg and S. Tretiak, Coherent exciton-vibrational dynamics and energy transfer in conjugated organics, *Nat. Commun.*, 2018, **9**, 2316–2324.

49 B. Lasorne, F. Sicilia, M. J. Bearpark, M. A. Robb, G. A. Worth and L. Blancafort, Automatic generation of active coordinates for quantum dynamics calculations : Application to the dynamics of benzene photochemistry, *J. Chem. Phys.*, 2008, **128**, 124307–124317.

50 M. Soler, A. Roitberg, T. Nelson, S. Tretiak and S. Fernandez-Alberti, Analysis of state-specific vibrations coupled to the unidirectional energy transfer in conjugated dendrimers., *J. Phys. Chem. A*, 2012, **116**, 9802–9810.

51 J. F. Galindo, S. Fernandez-Alberti and A. E. Roitberg, Electronic excited state specific IR spectra for phenylene ethynylene dendrimer building blocks, *J. Phys. Chem. C*, 2013, **117**, 26517–26528.

52 M. . Saab, L. J. . Doriol, B. . Lasorne, S. . Guerin and F. Gatti, A quantum dynamics study of the benzopyran ring opening guided by laser pulses., *Chem. Phys.*, 2014, **442**, 93−102.

53 B. Lasorne, G. a. Worth and M. a. Robb, Excited-state dynamics, *Wiley Interdiscip. Rev. Comput. Mol. Sci.*, 2011, **1**, 460–475.

54 J. C. Tully, Molecular dynamics with electronic transitions, *J. Chem Phys.*, 1990, **93**, 1061–1071.

55 S. Hammes-schiffer and J. C. Tully, Proton transfer in solution : Molecular dynamics with quantum transitions, *J. Chem Phys.*, 1994, **101**, 4657–4667.

56 S. Tretiak and S. Mukamel, Density matrix analysis and simulation of electronic excitations in conjugated and aggregated molecules, *Chem. Rev.*, 2002, **102**, 3171–3212.

57 V. Chernyak, M. F. Schulz, S. Mukamel, S. Tretiak and E. V Tsiper, Krylov-

space algorithms for time-dependent Hartree-Fock and density functional computations, *J. Chem. Phys.*, 2000, **113**, 36.

58 S. Tretiak, C. M. Isborn, A. M. N. Niklasson and M. Challacombe, Representation independent algorithms for molecular response calculations in time-dependent self-consistent field theories, *J. Chem. Phys.*, 2009, **130**, 054111–054127.

59 F. Furche and R. Ahlrichs, Adiabatic time-dependent density functional methods for excited state properties, *J. Chem. Phys.*, 2002, **117**, 7433–7448.

60 S. Tretiak and V. Chernyak, Resonant nonlinear polarizabilities in the time-dependent density functional theory, *J. Chem. Phys.*, 2003, **119**, 8809–8823.

61 M. Tommasini, V. Chernyak and S. Mukamel, Electronic density-matrix algorithm for nonadiabatic couplings in molecular dynamics simulations, *Int. J. Quantum Chem.*, 2001, **85**, 225–238.

62 V. Chernyak and S. Mukamel, Density-matrix representation of nonadiabatic couplings in time-dependent density functional (TDDFT) theories, *J. Chem. Phys.*, 2000, **8**, 3572–3579.

63 R. Send and F. Furche, First-order nonadiabatic couplings from time-dependent hybrid density functional response theory: Consistent formalism, implementation, and performance, *J. Chem. Phys.*, 2010, **132**, 044107–044119.

64 S. Mukamel, S. Tretiak, T. Wagersreiter and V. Chernyak, Electronic coherence and collective optical excitations of conjugated molecules, *Science (80-.).*, 1997, **277**, 781–787.

65 S. Tretiak, V. Chernyak and S. Mukamel, Recursive density-matrix-spectral-moment algorithm for molecular nonlinear polarizabilities, *J. Chem. Phys.*, 1996, **105**, 8914–8928.

66 S. Tretiak, W. M. Zhang, V. Chernyak and S. Mukamel, Excitonic couplings and electronic coherence in bridged naphthalene dimers, *Proc. Nat. Acad. Sci. USA*, 1999, **96**, 13003–13008.

67 M. J. S. Dewar, E. G. Zoebisch, E. F. Healy and J. J. P. Stewart, The development and use of quantum-mechanical molecular-models.76.AM1 - A new general purpose quantum-mechanical molecular-model, *J. Am. Chem. Soc.*, 1985, **107**, 3902–3909.

68 T. Nelson, S. Fernandez-Aberti, V. Chernyak, A. E. Roitberg and S. Tretiak, Nonadiabatic excited-state molecular dynamics modeling of photoinduced dynamics in conjugated molecules, *J. Phys. Chem. B*, 2011, **115**, 5402–5414.

69 T. Nelson, S. Fernandez-Alberti, V. Chernyak, A. E. Roitberg and S. Tretiak, Nonadiabatic excited-state molecular dynamics: numerical tests of convergence and parameters., *J. Chem. Phys.*, 2012, **136**, 054108–054120.

70 A. Davydov, *Theory of Molecular Excitons*, Plenum, New York, 1971.

71 V. Broude, E. Rashba and E. Sheka, *Spectroscopy of Molecular Excitons*, Springer, Berlin, 1985.

72 E. Y. Poliakov, V. Chernyak, S. Tretiak and S. Mukamel, Exciton-scaling and optical excitations of self-similar phenylacetylene dendrimers, *J. Chem. Phys.*, 1999, **110**, 8161–8175.

73 S. Tretiak, V. Chernyak and S. Mukamel, Two-dimensional real-space analysis of optical excitations in acceptor-substituted carotenoids, *J. Am. Chem. Soc.*, 1997, **119**, 11408–11419.

74 R. J. Bell, P. Dean and D. C. Hibbins-Butler, Localization of normal modes i n vitreous silica , germania and beryllium fluoride, *J. Phys. C Solid St. Phys*, 1970, **3**, 2111–2118.

75 S. N. Taraskin and S. R. Elliott, Anharmonicity and localization of atomic vibrations in vitreous silica, *Phys. Rev. B*, 1999, **59**, 8572–8585.

76 M. Soler, T. Nelson, A. Roitberg, S. Tretiak and S. Fernandez-Alberti, Signature of Nonadiabatic Coupling in Excited-State Vibrational Modes., *J. Phys. Chem. A*, 2014, **118**, 10372–10379.

77 S. Fernandez-Alberti, A. E. Roitberg, T. Nelson and S. Tretiak, Identification of unavoided crossings in nonadiabatic photoexcited dynamics involving multiple electronic states in polyatomic conjugated molecules., *J. Chem. Phys.*, 2012, **137**, 014512.

78 H. Chen, M. R. Golder, F. Wang, S. K. Doorn, R. Jasti, S. Tretiak and A. K. Swan, Raman-active modes of even-numbered cycloparaphenylenes: Comparisons between experiments and density functional theory (DFT) calculations with group theory arguments, *J. Phys. Chem. C*, 2015, **119**, 2879–2887.

79 J. Clark, T. Nelson, S. Tretiak, G. Cirmi and G. Lanzani, Femtosecond Torsional Relaxation, *Nat. Phys.*, 2012, **8**, 225–231.

80 D. Ondarse-Alvarez, N. Oldani, S. Tretiak and S. Fernandez-Alberti, Computational Study of Photoexcited Dynamics in Bichromophoric Cross-Shaped Oligofluorene, *J. Phys. Chem. A*, 2014, **118**, 10742–10753.

81 S. Tretiak, A. Saxena, R. Martin and A. Bishop, Conformational dynamics of photoexcited conjugated molecules, *Phys. Rev. Lett.*, 2002, **89**, 97402–97406.

82 S. Karabunarliev, M. Baumgarten, E. Bittner and K. Mullen, Rigorous Franck Condon Absorption and Emission Spectra of Conjugated Oligomers from Quantum Chemistry., *J. Chem. Phys.*, 2000, **113**, 11372–11381.

83 I. Franco and S. Tretiak, Electron-vibrational dynamics of photoexcited polyfluorenes, *J. Am. Chem. Soc.*, 2004, **126**, 12130–12140.

84 H. E. Zimmerman and I. V. Alabugin, Excited state energy distribution and redistribution and chemical reactivity; mechanistic and exploratory organic photochemistry, *J. Am. Chem. Soc.*, 2000, **122**, 952–953.

85 J. H. Kim, A. R. T. Nugraha, L. G. Booshehri, E. H. H??roz, K. Sato, G. D. Sanders, K. J. Yee, Y. S. Lim, C. J. Stanton, R. Saito and J. Kono, Coherent phonons in carbon nanotubes and graphene, *Chem. Phys.*, 2013, **413**, 55–80.

86 Y.-S. Lim, A. R. T. Nugraha, S.-J. Cho, M.-Y. Noh, E.-J. Yoon, H. Liu, J.-H. Kim, H. Telg, E. H. Hároz, G. D. Sanders, S. H. Baik, H. Kataura, S. K. Doorn, C. J. Stanton, R. Saito, J. Kono and T. Joo, Ultrafast Generation of Fundamental and Multiple-Order Phonon Excitations in Highly Enriched (6,5) Single-Wall Carbon Nanotubes, *Nano Lett.*, 2014, **14**, 1426–1432.

87 Y.-S. Lim, K.-J. Yee, J.-H. Kim, E. H. Hároz, J. Shaver, J. Kono, S. K. Doorn, R. H. Hauge and R. E. Smalley, Coherent Lattice Vibrations in Single-Walled Carbon Nanotubes, *Nano Lett.*, 2006, **6**, 2696–2700.

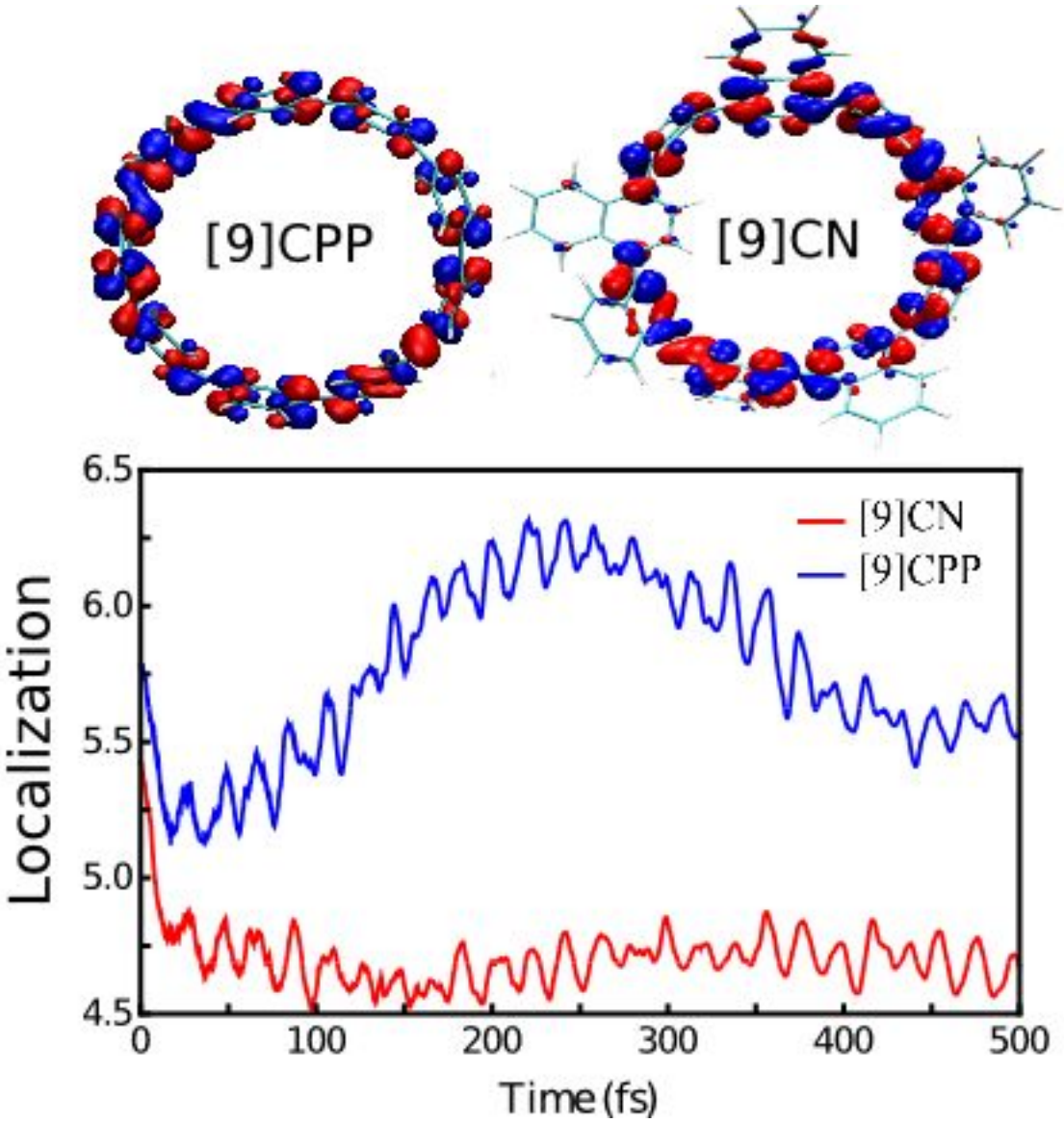

Electronic energy relaxation takes place through specific sets of active normal modes within similar narrow ranges of middle- to high-frequencies.